

Analysis and Simulation of Dynamic Characteristics for Multi-Split Transmission Line Splicing Pipe Flaw Detection Robot

Dehua ZOU^{a,b}, Zhipeng JIANG^{a,b}, Minmin QIAO^{a,b}, Lanlan LIU^{a,b}, Wei JIANG^{c,1} and Qianwei YI^d

^aHunan Province Key Laboratory of Intelligent Live Working Technology and Equipment (ROBOT) (State Grid Hunan EHV Transmission Company), Changsha, Hunan, 410100 China

^bLive Inspection and Intelligent Operation Technology State Grid Corporation Laboratory (State Grid Hunan EHV Transmission Company), Changsha, Hunan, 410100 China

^cWuhan Textile University, Hubei Key Laboratory of Digital Textile Equipment, Wuhan 40200, China

^dThree Gorges University, College of International Communications, Yichang 443000, China

Abstract. The splicing pipe is an important hardware on multi-split transmission lines. The quality of its crimping and internal structure directly affects the normal and stable operation of the transmission line. The online flaw detection robot for the splicing pipe is an important means to realize the automatic flaw detection of the splicing pipe. This paper on the basis of proposing a robot mechanism configuration suitable for multi-split transmission line splicing pipe flaw detection, aiming at the matching relationship between the imaging plate movement and the mechanism joint driving torque during the splicing pipe flaw detection process, a flaw detection method is established by using the Lagrangian method. The dynamic model of the operation process of the imaging board is installed, and the relationship between the joint motion of each mechanism and the pose change of the imaging board in the area under the jurisdiction of the four-split wire is analyzed. The displacement and velocity curves of each joint motion of the robot can be obtained. From the simulation results, it can be known that the joint motion of the robot is continuous and stable, and the motion of the imaging plate is driven continuously and smoothly, which realizes the coordinated pose control between the imaging probe and the imaging plate. Coupling pipe flaw detection operation, the research in this paper has important theoretical significance and practical application value for the design of the transmission line joint pipe flaw detection robot system, especially the joint drive mechanism design.

Keywords. Multi-split power transmission wire, flaw detection, robot, imaging plate movement, dynamic characteristics

¹ Wei Jiang, Corresponding author, Wuhan Textile University, Hubei Key Laboratory of Digital Textile Equipment, Wuhan 40200, China; E-mail: jiangwei2013@whu.edu.cn.

1. Introduction

Splicing tube [1-2] is common hardware used to connect transmission wires on high-voltage transmission lines, and its operation condition and internal structure are directly related to the safe and stable operation of the line. However, the transmission line service in the harsh natural environment, a long time of wind, sun, and rain, the performance of the tube will be greatly reduced, and even faults such as deformation and heating can occur, while the quality of the splicing tube is a hidden project [5-6], with the naked eye is difficult to judge the crimping effect, therefore, the development of the transmission line crimp tube flaw detection automatic monitoring equipment has important theoretical significance and practical application value. In the process of splicing tube detection by positioning the splicing tube, while with the splicing tube flaw detection device detection probe and the movement of the imaging plate, the splicing tube is placed between the imaging plate and the detection probe of the splicing tube, where the movement of the imaging plate is driven by the joint motion of the mechanism, the size of the driving torque is directly related to the movement of the imaging plate in the detection process. Therefore, by establishing the dynamics model of the splicing tube inspection mechanism, the analysis and simulation of the model to obtain the drive torque of the mechanical joint that can drive the flexible movement of the imaging plate is the key to completing the automatic inspection of the splicing tube flaw detection. There are various modeling methods for robot dynamics, among which reducing the computational complexity of multi-degree-of-freedom robot dynamics models is a hot topic of current research [3-4]. Meanwhile, obtaining the mechanical properties of robot joint drives through robot dynamics models and realizing the mapping relationship between dynamics models and dynamics parameters are also important aspects of research in the field of robot dynamics [5-6].

To sum up the above, this paper takes the multi-divided transmission conductor splicing tube intelligent electric flaw detection device as the system platform and research object, by establishing the dynamics model of imaging plate motion during the flaw detection operation, and importing the 3D solid model in ADAMS software for dynamics simulation research, to obtain the optimal driving parameters of the imaging plate mechanism joint motion, compared with the general motion of traditional robots and robotic arms, the motion characteristics of the splicing tube detection device in the narrow area of the four split wires play an important role in the successful completion of the flaw detection operation, the research in this paper has important theoretical significance and practical application value for the design of the automatic detection system of the splicing tube flaw detection.

2. Design of Splicing Tube Flaw Detection Robot System

The flaw detection device designed in this paper can be divided into two main parts which are the infrared ray machine carried by the UAV and the flaw detection device, they are distributed up and down and connected to the flaw detection device by a straddle mount. The role of the UAV is to carry the flaw detection device to a high altitude and use the ray machine with the flaw detection device to detect the splicing tube, its structure is a six-rotor UAV, each wing carries a propeller, and each wing and the UAV connection has a rotating joint, to be fixed on the flaw detection device on the four split wire, its wings will contract. The infrared ray machine is erected in the

middle hollow of the UAV through a bracket, and the angle of the ray machine is adjusted through the ray machine flip joint. The main body of the detection device is divided into a fixed device and an imaging device, the fixed device includes four brackets, four rectangular pressure blocks, and two clamping blocks on both sides, the clamping block has a rotating joint, and the role is used to clamping the wire when the detection device is placed on the wire. The imaging device includes putter, slider, and imaging plate, where the putter has a rotary joint fixed on the rectangular block, and a telescopic joint can control the lower imaging plate rotary joint to adjust the angle of the imaging plate, and the imaging plate lift joint and translation joint can adjust the height and distance of the imaging plate so that the imaging plate in the appropriate position from the splicing tube.

3. Dynamics Theoretical Modeling of the Inspection Robot

3.1. Establishment of the Coordinate System

The key to completing the detection of multi-split transmission line splicing tube is the movement of the imaging plate driven by the joint movement of the mechanism with the movement of the scanning probe to achieve the infrared detection of transmission line splicing tube, according to the basic mechanical configuration of the transmission line online inspection device can establish the dynamics of the device model coordinates as shown in figure 1. At point A to establish the coordinate system, X_0 direction for 1, 2 connecting rod horizontal extension direction, Y_0 direction for the vertical upward direction of the connecting rod, Z_0 direction perpendicular to the right side of the connecting rod extension direction. The meanings of each parameter are: l is the length of the connecting rod, I is the rotational inertia of the rotating rod, θ_1 and θ_2 are the rotation angles between connecting rod 1 and point A and connecting rod 2 and rod 1, respectively, r is the displacement variable of the telescopic rod mass, m is the mass of the connecting rod, T is the joint driving torque.

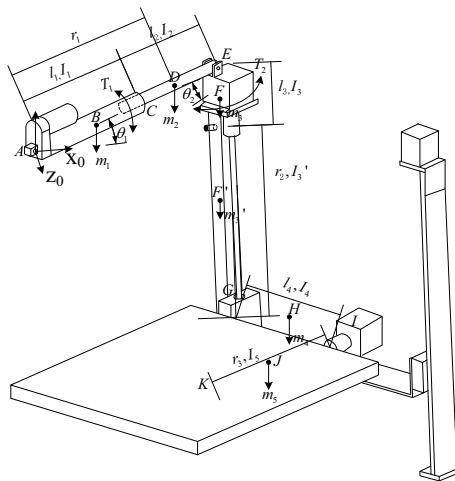


Figure 1. Coordinate model of imaging plate joint motion dynamics.

3.2. Kinetic Model of the Imaging Plate

Robot dynamics theory is most commonly modeled using the Lagrange dynamics equation, which is shown in Eq. 1. Where K is the kinetic energy of the system, P is the potential energy of the system, and the combined external moment is shown in Eq. 2.

$$L = \sum_{i=1}^i K_i - \sum_{i=1}^i P_i \tag{1}$$

$$T_i = \frac{\partial}{\partial t} \left(\frac{\partial L}{\partial \dot{\theta}_i} \right) - \frac{\partial L}{\partial \theta_i} \tag{2}$$

The expressions of kinetic energy, potential energy, and rotational inertia during the motion of the imaging plate and connecting rod are shown in Eq. 3, Eq. 4 and Eq. 5.

$$\begin{cases} K_1 = \frac{1}{2} I_1 \dot{\theta}_1^2 \\ K_2 = \frac{1}{2} I_2 \dot{\theta}_2^2 \\ K_3 = \frac{1}{2} I_3 \dot{\theta}_3^2 \\ K'_3 = \frac{1}{2} I'_3 \dot{\theta}_3^2 \\ K_4 = \frac{1}{2} I_4 \dot{\theta}_4^2 + \frac{1}{2} m_4 v_4^2 \\ K_5 = \frac{1}{2} I_5 \dot{\theta}_5^2 + \frac{1}{2} m_5 v_5^2 \end{cases} \tag{3}$$

$$\begin{cases} P_1 = m_1 g \frac{1}{2} l_1 \sin \theta_1 \\ P_2 = m_2 g r_1 \sin \theta_1 \\ P_3 = m_3 g h_1 \\ P'_3 = m'_3 g h_2 \\ P_4 = m_4 g h_4 \\ P_5 = m_5 g h_4 \end{cases} \tag{4}$$

$$\begin{cases} I_1 = \frac{1}{3} m_1 l_1^2 \\ I_{i=2:5} = \frac{1}{12} m_i l_i^2 \end{cases} \tag{5}$$

Where in $\theta_3 = \pi - \theta_1 - \theta_2$, for the convenience of analysis, the 3D model diagram is expanded along the x-y direction, the plane diagram is shown in figure 2, and the h obtained by calculation is shown in Equation 6.

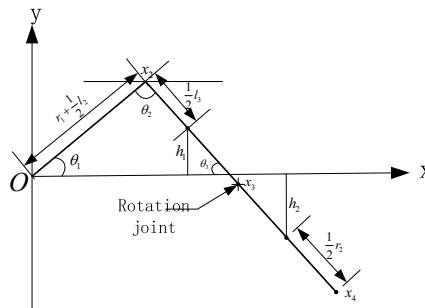


Figure 2. Motion plane model of the imaging plate system.

$$\begin{cases} h_1 = (r_1 + \frac{1}{2}l_2) \sin \theta_1 - \frac{1}{2}l_3 \sin \theta_3 \\ h_2 = (\frac{1}{2}l_3 - \frac{r_1}{\sin \theta_3} + \frac{1}{2}r_2) \sin \theta_3 \\ h_4 = -(h_2 + \frac{1}{2}r_2 \sin \theta_3) \end{cases} \quad (6)$$

V4 is determined by differentiating the 3-D position vector, and the position representation and velocity representation are shown in Eq. 7 and Eq. 8, and V5 can be calculated in the same way.

$$\begin{cases} x_4 = (r_1 + \frac{l_2}{2}) \cos \theta_1 + \frac{l_3}{2} \cos \theta_3 + \frac{(h_1 + h_2)}{\tan \theta_3} + \frac{r_2}{2} \cos \theta_3 \\ y_4 = -(h_2 + \frac{r_2}{2}) \\ z_4 = \frac{l_4}{2} \end{cases} \quad (7)$$

$$\begin{cases} \dot{x}_4 = (\dot{r}_1 + \frac{\dot{l}_2}{2}) \cos \theta_1 - (\dot{r}_1 + \frac{\dot{l}_2}{2}) \dot{\theta}_1 \sin \theta_1 - \frac{\dot{l}_3}{2} \dot{\theta}_3 \sin \theta_3 + \frac{l_3}{2} \frac{-\dot{\theta}_3}{\sin^2 \theta_3} + \dot{r}_2 \cos \theta_3 - r_2 \dot{\theta}_3 \sin \theta_3 \\ \dot{y}_4 = -\left[\frac{\dot{l}_2}{2} - \left[(\dot{r}_1 + \frac{\dot{l}_2}{2}) \sin \theta_1 + (r_1 + \frac{l_2}{2}) \dot{\theta}_1 \cos \theta_1 \right] + \frac{\dot{l}_3}{2} \dot{\theta}_3 \cos \theta_3 + \left[\frac{\dot{r}_2}{2} (\sin \theta_3 + 1) + \frac{r_2}{2} \dot{\theta}_3 \cos \theta_3 \right] \right] \\ \dot{z}_4 = 0 \end{cases} \quad (8)$$

$$\begin{aligned} v_4^2 = \dot{x}_4^2 + \dot{y}_4^2 = & \left[0.5l_3 - (0.5l_2 + r_1) \sin \theta_1 + 0.5r_2 (\sin(\theta_1 + \theta_2) + 1) - \dot{\theta}_1 (0.5l_2 + r_1) \cos \theta_1 + 0.5(l_2 + l_3) \cos(\theta_1 + \theta_2) (\dot{\theta}_1 + \dot{\theta}_2) \right]^2 \\ & + \left[(0.5l_2 + r_1) \cos \theta_1 - r_2 \cos(\theta_1 + \theta_2) + \left(\frac{l_3(\dot{\theta}_1 + \dot{\theta}_2)}{2 \sin(\theta_1 + \theta_2)} \right) - \dot{\theta}_1 (0.5l_2 + r_1) \sin \theta_1 + (0.5l_2 + r_2) \sin(\theta_1 + \theta_2) (\dot{\theta}_1 + \dot{\theta}_2) \right]^2 \end{aligned} \quad (9)$$

The dynamical model of the system is obtained by substituting the known expressions to solve the Lagrange dynamics equations and differentiating the driving moments.

4. ADAMS-based Simulation of the Dynamics

4.1. Simulation Platform Construction and Parameter Configuration

The 3D geometric model drawn in Inventor was exported to .STP format, which was imported into ADAMS, and a modular Boolean operation of the model was performed to integrate the entire device not involved in the imaging operation with the Boolean operation, leaving the imaging camera above and the imaging device below. The operation simulation is performed for the lower motion linkage and camera. For simplicity of analysis, the material properties are all set to steel. The motion subsets are added according to each linkage action in the operation planning device. The linkage

action needs to add the driving drive, set the imaging detection sequence from the lower-left corner of the wire, the lower right corner, the upper left corner, to the end of the upper right corner, plan the running time of 15s, Where UAV is the UAV, under is the device below not involved in dynamics modeling, and up is the imaging camera above, the dynamics simulation diagram built is shown in figure 3.

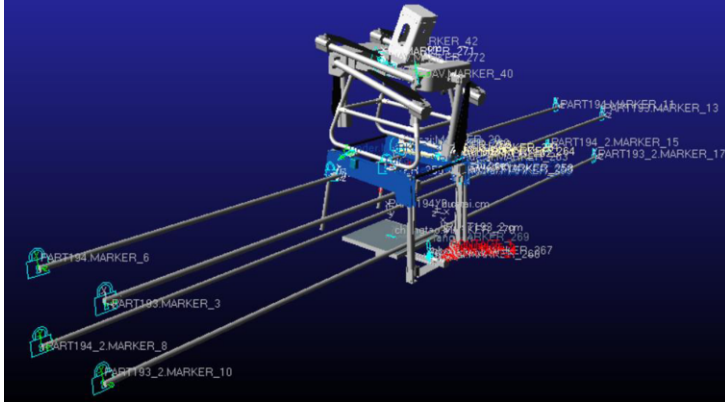


Figure 3. The effect of the simulation constraint built in ADAMS.

4.2. Motion Characterization

To further study the kinetic characteristics of the moving process for the splicing tube detection device, the velocity and displacement characteristics of the imaging plate at the end of the device need to be analyzed. The velocity variation characteristics of the imaging plate are shown in figure 4. The whole motion of the imaging device is carried out in the XOY plane, and after the simulation starts, within 0-1.0s, the imaging plate rotates from the initial position to the lower left side of the wire, and since the rotation is carried out in the XOY plane, only V_x , V_y , V_x increases from 0 to maximum -43.655 and decreases to 0, V_y increases from 0 to maximum 32.0198 decreases to 0, $V_z = 0$; in 2.0-3.0s, the imaging plate makes a translational motion to the right along the x-direction, so only V_x exists, V_x max 434.9539; in 5.0-6.0s, after the end of detecting the wire below, the slide table drives the imaging plate to rotate in the XOY plane to the right of the wire, V_x max 978.9236, due to the lever motion In 6.5-7.5s, the imaging plate moves upward along the slide table, and since it is tilted, V_x is -607.1281 and V_y is -97.6974. In 8.0-9.0s, the slide table drives the imaging plate to rotate to a horizontal position. In 8.0-9.0s, the sliding table rotates the imaging plate to the horizontal position, the same as the 5.0-6.0s state, it needs to rotate from below and enter, so there is also a short change of velocity in -y direction, and then it changes to +y direction. After waiting for 0.5s, i.e., within 9.5-10.5s, the imaging plate moves horizontally to the left with a maximum velocity of -434.9539; within 12.5-13.5s, the imaging plate moves horizontally to the right with a maximum velocity of 434.9539, and the movement of the imaging plate ends here.

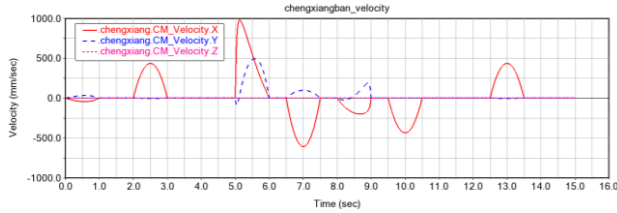


Figure 4. Speed characteristics.

The characteristics of the displacement changes in the three dimensions of the imaging plate are shown in figures 5, 6, and 7, respectively. In 0-2s, the imaging plate has a weak rotation, so both x- and y-direction displacements exist, and the x-direction displacement has a brief decrease with a change of -29.9815mm, and the y-direction has a brief increase with a change of +21.1567mm. 2-3s, the imaging plate moves horizontally along the x-positive direction and the x-direction displacement changes by 289.9983mm. 5-6s, The imaging plate rotates out from below, the x-direction displacement increases by 518.5976 mm, and the y-direction displacement first moves by 5.9329 mm in the -y direction and then increases to 199.4841 mm in the y direction, for a total displacement of 291.2671 mm. 6.5-7.5s, the imaging plate moves upward along the slide, and because it moves at an angle, there are three directions of displacement, and the x-direction displacement decreases from 778.6114 mm to 373.8189 mm, the y-direction displacement increases from -199.4841 mm to -134.346 mm, and the z-direction displacement increases from -147.1993 mm to -147.0571 mm. 8.0-9.0s, the slide table drives the imaging plate to rotate to the left side to the horizontal position, the x-direction displacement decreases, decreasing by 142.993mm, and because it is rotated into, the y-direction displacement first decreases and then increases, finally increasing to -81.7637mm. Within 9.5-10.5s, the imaging plate moves horizontally to the left, and the x-direction displacement continues to decrease, from 230.8259mm to -59.1723mm. Within 12.5-13.5s, the imaging plate moves horizontally to the right, and the x-direction displacement increases to 230.8259 mm. The whole process was following the detection motion planning of the splice tube, and the validity of the dynamics model was verified.

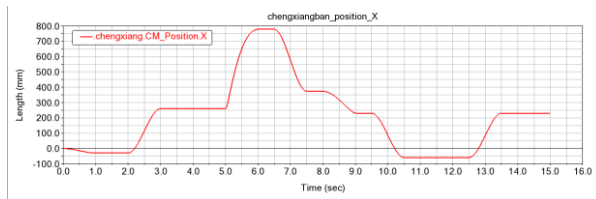


Figure 5. Displacement variation of the imaging plate in the X-axis direction.

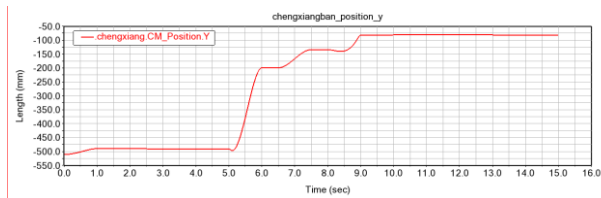


Figure 6. Displacement change of the imaging plate in the Y-axis direction.

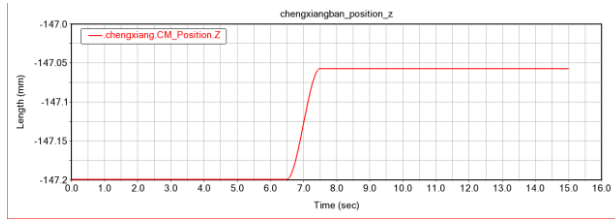


Figure 7. Displacement variation of the imaging plate in the Z-axis direction.

5. Conclusion

(1) Regarding the online inspection of the internal crimping quality of the multi-divided transmission line splicing tube, a new method is proposed that can adapt to the four-divided transmission conductors, drive the movement of the imaging plate through the mechanism joint movement, and adjust the probe and imaging plate position relationship to achieve transmission line splicing tube inspection.

(2) The motion process of the imaging plate during the detection of the splicing tube is studied, and the dynamics model of the imaging plate with joint motion is established based on the Lagrange method, and the mechanical characteristics of the operation process of the splicing tube detection device are analyzed.

(3) By importing the 3D model, the motion state of each joint during the motion of the imaging plate was simulated and analyzed in ADAMS software, and the displacement and velocity curves of each joint were obtained, and the results showed that the joint motion could drive the smooth and continuous motion of the imaging plate.

Acknowledgement

This project was supported by Science and Technology Project of State Grid Hunan Electric Power Corporation (No. 5216AJ210005).

Reference

- [1] Menendez O, Cheein FAA, Perez M, et al. Robotics in power systems: Enabling a more reliable and safe grid. *IEEE Industrial Electronics Magazine*. 2017; 11(2): 22-34.
- [2] Jalal MFA, Sahari KSM, Fei HM, et al. Design and development of three arms transmission line inspection robot. *Journal of Robotics, Networking and Artificial Life*. 2018; 5(3): 157-160.
- [3] Wang W, Wu G, Bai Y, et al. Hand-eye-vision based control for an inspection robot's autonomous line grasping. *Journal of Central South University*. 2014; 21(6): 2216-2227.
- [4] Shruthi CM, Sudheer AP, Joy ML. Optimal crossing and control of mobile dual-arm robot through tension towers by using fuzzy and Newton barrier method. *Journal of the Brazilian Society of Mechanical Sciences and Engineering*. 2019; 41(6): 245-270.
- [5] Alhassan AB, Zhang X, Shen H, et al. Investigation of aerodynamic stability of a lightweight dual-arm power transmission line inspection robot under the influence of wind. *Mathematical Problems in Engineering*. 2019; 2139462.
- [6] Zhao T, Chen Y, Dian S, et al. General type-2 fuzzy gain scheduling PID controller with application to power-line inspection robots. *International Journal of Fuzzy Systems*. 2020; 22(1): 181-200.